

The ESO-Sculptor Faint Galaxy Survey: Large-Scale Structure and Galaxy Populations at $0.1 \lesssim z \lesssim 0.5^*$

V. DE LAPPARENT, G. GALAZ, S. ARNOUITS, CNRS, Institut d'Astrophysique de Paris
S. BARDELLI, M. RAMELLA, Osservatorio Astronomico di Trieste

1. Introduction

We describe the current status of the ESO-Sculptor Survey. The observational goal has been to produce a new multi-colour photometric catalogue of galaxies in a region located near the southern galactic pole, complemented by a spectroscopic survey. The primary scientific objectives are (1) to map the spatial distribution of galaxies at $z \approx 0.1$ – 0.5 and (2) to provide a database for studying the variations in the spectro-photometric properties of distant galaxies as a function of redshift and local environment. The first clues towards the understanding of the matter distribution in the Universe have been obtained by mapping the distribution of its major light-emitting components, the galaxies. One of the main properties of the galaxy distribution is the presence of structures at nearly the largest scales examined (of the order of $100 h^{-1}$ Mpc with a Hubble constant of $H_0 = 100 h \text{ km s}^{-1}$) Mpc. The 3-dimensional maps provided by redshift surveys of various regions of the sky have clearly demonstrated the inhomogeneity of the galaxy distribution and have emphasised the need for systematic redshift surveys over large volumes of the universe.

The nearby galaxy distribution suggests a remarkable structure in which galaxies cluster along sharp walls which delineate vast regions with diameters between 10 and $50 h^{-1}$ Mpc devoid of bright galaxies, in a cell-like pattern [2]. Gigantic structures such as the “Great Wall” have been detected and pose the problem of the largest scale for the inhomogeneities [3]. The general distribution has the topological properties of a “sponge”, which naturally arises from gaussian initial perturbations collapsing under gravity. The nearby redshift maps [2] have generated a renewed interest in mapping the large-scale structure of the Universe in the early 1990's. Several ambitious programmes were then initiated and provide new maps which probe the distribution out to distances of $\sim 500 h^{-1}$ Mpc. These maps contain many sheets and voids, and confirm the sponge-like topology [4, 5], with no evidence of voids larger than $\sim 100 h^{-1}$ Mpc [6]. It seems that these surveys have reached the scale where the galaxy distribution becomes homogene-

ous, but this requires further quantitative studies.

The maps of the galaxy distribution raise several fundamental questions of observational cosmology. Among them is the problem of the missing mass detected in increasing amounts at larger and larger scales [7]. If the limits of the nucleosynthesis predictions are to be met [8], the required dark matter for explaining the formation of large-scale structure must be for the most part non-baryonic [9]. In this picture, the galaxy formation must be biased towards the densest peaks of the matter distribution [10]. Therefore, the voids of the galaxy distribution could be filled with dark – and partly non-baryonic – matter. So far, all observational searches for baryonic matter within these voids in the form of galactic-size systems have led to only rare detections (see [11, 12] and references therein), largely insufficient for explaining a significant fraction of the missing mass. The detection of the dark matter is therefore a crucial requirement for validating the current scenario for large-scale-structure formation (the gravitational collapse of primordial fluctuations). Another challenge is to reconcile the size and amplitude of the inhomogeneities in the galaxy distribution with the high degree of isotropy of the microwave background radiation [13] (this also requires large amounts of dark matter).

Mapping the inhomogeneities in the galaxy distribution allows to obtain clues on the nature of the primordial fluctuations in the matter density field, and therefore to better understand the prevailing mechanisms in shaping the early universe. At large scales, constraints on the spectrum of primordial fluctuations can be derived directly from the maps of the 3-dimensional galaxy distribution. On smaller scales ($\sim 1 h^{-1}$ Mpc), the non-linear effects of gravitation compli-

cate the derivation of such constraints. A study of the different galaxy populations and their environment becomes necessary for a better insight into the formation of structure on galactic size up to several h^{-1} Mpc. Constraints on the initial perturbations which led to the formation of structures on these scales may be obtained if one can eventually make the link between the mass function of the collapsing matter, the star formation history of the galaxies, and the influence of their environment. The mass function is predicted by the theoretical models and is partly constrained by the galaxy luminosity function [14]. The star formation history is tightly constrained by the observations (spectral energy distribution and magnitude number counts) [15]. One difficulty is to decouple the influence of the local environment, to which galaxies are intimately related via tidal interactions and mergers, from the large-scale segregation effects resulting from the initial conditions [16].

Detailed knowledge of both the large-scale clustering and the galaxy populations in a 3-dimensional galaxy map therefore provides invaluable information for studying the formation and evolution of structure in the universe. With the goal to address these issues, the ESO-Sculptor survey of faint galaxies (ESS, hereafter) was initiated in 1989. The programme was granted the key-programme status by ESO, which provided the unique opportunity for obtaining a new complete galaxy sample to both substantial depth and area on the sky. A large amount of observing nights on the 3.6-m and NTT was attributed and allowed to complete the observations in the fall of 1995. We describe the characteristics of the photometric and spectroscopic ESS samples in § 2 and 3 respectively, and we report the major results already obtained in § 4. In § 5 we

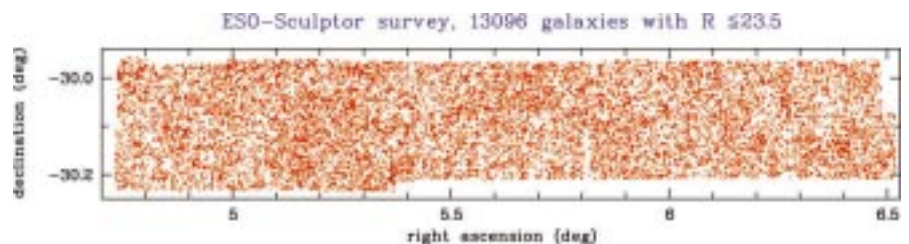


Figure 1: Distribution on the sky of the 13,096 galaxies in the ESO-Sculptor Survey (ESS) to its completeness limit of $R = 23.5$ (in J2000 equatorial co-ordinates). The r.m.s. magnitude uncertainties are 0.04 mag, and the r.m.s. astrometric uncertainties are ~ 0.2 arcsec. Even at this large depth, the galaxy distribution shows large-scale inhomogeneities which are measured by the angular 2-point correlation function [19].

*The ESO-Sculptor Faint Galaxy Survey is one of the ESO Key Programmes. All the data have now been collected.

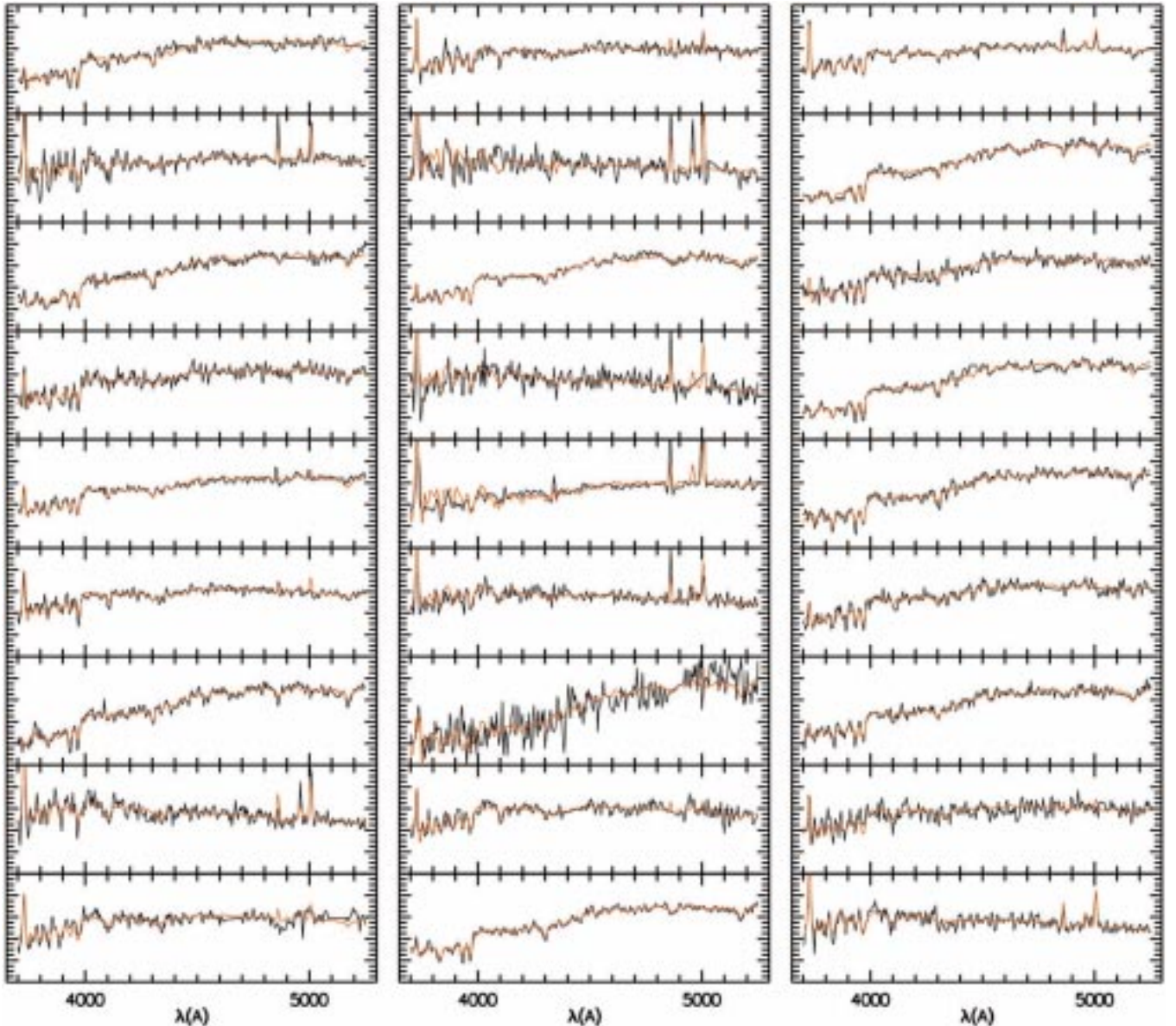


Figure 2: 27 spectra from the ESS (black curves) and their reconstructions using 3 principal components (red curves; see text for details). Note the filtering effect on the spectra with low signal-to-noise ratio, and the variable accuracy in the reconstruction of spectral lines.

comment on the results and examine the prospects for the ESS in the coming years.

2. The ESS Photometric Sample

The photometric data for the ESS [17] was obtained from CCD imaging of a continuous strip of 1.53° (R.A.) \times 0.24° (DEC.) ≈ 0.37 deg² in the Sculptor constellation ($\sim 0^h 21^m$, $\sim -30^\circ$ in J2000 coordinates), 17° away from the Southern Galactic Pole. The typical exposure times at the NTT in the *B*, *V*, *R* filters were 25 min, 20 min, and 15 min, respectively. Whereas the *R* and *V* images have comparable depths, the *B* images are shallower because of the lower quantum efficiency at short wavelengths of the CCDs used. The photometry for the survey is obtained by a mosaic of ~ 50 CCD frames in each filter overlapping on the edges. The galaxy catalogues are complete to $B = 24.5$, $V = 24$ and $R =$

23.5. All objects are detected in the 3 bands up to $R \sim 21.5$. In the range $22 < R < 23.5$, the colour completeness drops to 65%. Figure 1 shows the projected distribution on the sky for the *R* photometric sample.

The data were reduced within MIDAS on SUN and IBM workstations. The major steps in the data reduction were: bias subtraction, flat-fielding using a “super-flat” obtained from median-filtering of the target exposures themselves, co-addition of multiple exposures, removal of cosmic events. Because the photometric data were obtained during 10 different observing runs with changing telescopes, instruments, filters and detectors, the calibration of the data required a thorough work of measurement of colour coefficients and magnitude zero-points. These were determined simultaneously with an iterative method. Listed in Table 1 are the mean zero-points and the colour coefficients for the

various instrumental set-ups used at the 3.6-m (EFOSC1) in 1989–1990, and at the NTT (EMMI) from 1990 to 1995 (see [17] for further details). These allow to convert the observed CCD magnitudes into the standard Johnson-Cousins *BVR* system.

To obtain a homogeneous photometry, an algorithm for comparing and adjusting the measured magnitudes in the overlaps of neighbouring CCD frames was used [17]. This technique reduces by a factor of 3 the systematic deviations in zero-point between individual CCD frames. The resulting r.m.s. internal uncertainties in our photometry are 0.04 mag in the 3 filters. The galaxy catalogue was obtained by analysing the full CCD data with SExtractor [18]. Note that the ESO-Sculptor data played a major role in testing and improving the performances of the SExtractor package for faint galaxy photometry. Because of its excellent performances, this software is

now widely used by the astronomical community. The final ESS photometric catalogue was produced after identification of the multiple detections of the same objects from different images, and determination of the adopted object parameters. This catalogue provides aperture magnitudes in the standard B (Johnson), V (Johnson) and R (Cousins) filters, astrometric positions to 0.2 arcsec, and morphological parameters for ~ 9500 , $\sim 12,150$, and $\sim 13,000$ galaxies, respectively [17, 19]. As a by-product, the ESS also provides the 3-colour photometry of 2143 stars to $B = 24.5$. These are useful for constraining the models of galactic structure.

The ESO-Sculptor galaxy number-counts in the 3 bands, and the colour distributions are in good agreement with the results for other existing samples [17]. The faint number counts show the well-known excess over no-evolution models, in all 3 bands [20]. The faintest galaxies also exhibit a colour evolution, characterised by a blueing trend at $R > 22$ in the $B - V$ colour. These effects are often interpreted as an increase in the star-formation rate with look-back time [20]. The angular 2-point correlation function also shows evidence for significant evolution at $R \approx 23$ which could be related in origin to the excess of faint galaxies in the blue number-counts [19]. Whereas the change in amplitude at fainter magnitudes was already detected in several other samples, a change in the slope is also detected thanks to the increased survey area compared to the previous studies [19]. This analysis of the angular 2-point correlation function might provide new clues on the nature and evolution of galaxies at faint magnitudes. Adjustment of the number-counts, colour distributions, and variations in the slope and amplitude of the two-point correlation function for the ESS provide useful constraints for the models of galaxy evolution, and might allow to discriminate among the different scenarios (pure luminosity evolution,

dwarf galaxy component, etc.) [20].

3. The ESS Spectroscopic Sample

The spectroscopic catalogue provides the flux-calibrated spectra of the complete subsample of ~ 700 galaxies with $R_c \leq 20.5$ using multi-slit spectroscopy. At this depth, there are 1.3 galaxy per sq. arcmin in the survey, and the typical multi-slit masks at the NTT contain ~ 30 slits. The spectra are reduced using semi-automatic MIDAS procedures which were specifically designed for these data and which guarantee a homogeneous and systematic treatment of the numerous CCD exposures and extracted spectra. The major steps in the spectroscopic reduction are: 2-D correction for vignetting of field; cosmic events removal by comparison of multiple exposures; flat-fielding to correct for pixel-to-pixel variations, for variations in the slits transmission, and for fringes; long-slit wavelength calibration using the context LONG of MIDAS; sky subtraction with a wavelength-dependent fit of the sky flux along the slit and by interpolation at the position of the object; optimal extraction of objects by profile weighting; flux calibration using

ESO-Sculptor survey, 430 galaxies with $R \leq 20.5$

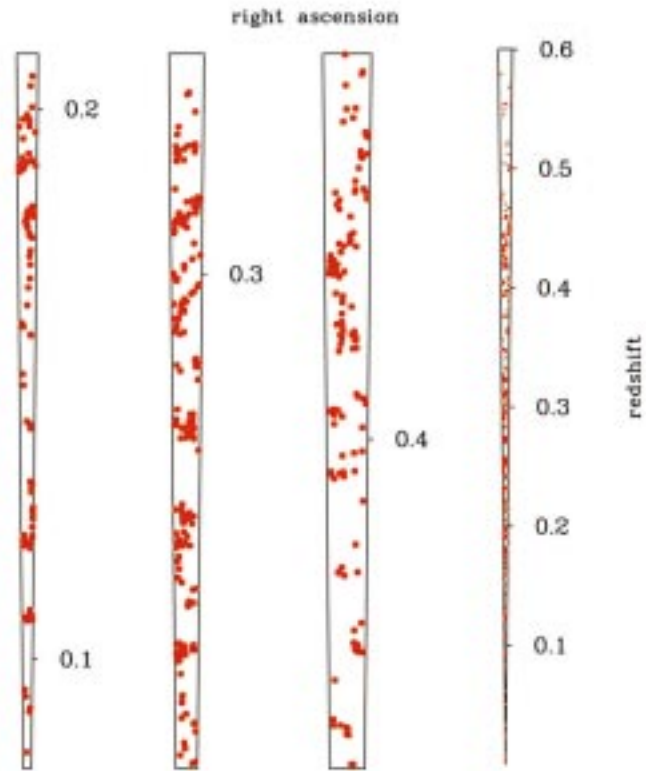


Figure 3: Distribution in R.A. versus redshift for 402 galaxies in the ESS in 3 contiguous redshift ranges (0.08–0.21, 0.21–0.34, 0.34–0.47). These maps show that the alternation of voids and walls persist at large distances, with a typical scale of $20\text{--}60 h^{-1} \text{Mpc}$ [25]. The right-most cone shows the geometry of the full volume of the ESS (430 galaxies). In all 4 cones, the right ascension range is $4.72\text{--}5.9^\circ$ (see Figure 1).

spectrophotometric standards; cross-correlation of the resulting spectra with galaxy templates for redshift measurement and error estimation.

The delicate extraction of spectra of extended objects with an integrated luminosity which represents only a fraction of the night sky, as it is the case for the ESS, requires optimised techniques. As a result, several of the high-level commands have been re-written within

Table 1: CCD photometric characteristics for EFOSC1 (3.6-m) and EMMI (NTT)

Instrument CCD/Period	Average zero-points			Colour coefficients ^(a)			
	B	V	R	$k_B[B-V]$	$k_V[B-V]$	$k_V[V-R]$	$k_R[V-R]$
EFOSC1 RCA#8/43-44 RCA#8/45-46	23.70 ± 0.03 23.41 ± 0.01	24.24 ± 0.04 24.06 ± 0.03	24.21 ± 0.02 24.03 ± 0.02	0.16 ± 0.03 0.16 ± 0.03	0.04 ± 0.02 0.04 ± 0.00	0.10 ± 0.02 0.10 ± 0.02	0.00 ± 0.02 0.00 ± 0.02
EMMI-R THX#18/49-50 LOR#34/52 TEK#36/54	24.69 ± 0.02	24.30 ± 0.02 25.40 ± 0.02	24.65 ± 0.03 25.14 ± 0.02		0.05 ± 0.01 0.03 ± 0.02	0.10 ± 0.02 0.05 ± 0.02	-0.10 ± 0.01 -0.03 ± 0.01
EMMI-B TEK#31/52 TEK#31/54	24.69 ± 0.02 24.26 ± 0.01			-0.21 ± 0.02 -0.21 ± 0.02			

(a) Indicated in brackets are the colour terms by which must be multiplied the listed coefficients k_M in order to convert the observed CCD magnitudes M_{obs} into the standard Johnson-Cousins magnitudes M_{std} ($M_{std} = M_{obs} + k_M \text{colour}$).

MIDAS, and allow better control of the reduction. In particular, the cross-correlation programme was specifically written for and tested on the ESS data. The essential steps are the continuum subtraction, the filtering of the spectra, and the matching of the rest-wavelength intervals of the observed spectrum and template. This matching is performed by first estimating the object redshift based on the cross-correlation with 6 templates representing the different galaxy spectral types (E, S0, Sa, Sb, Sc, Irr) and obtained by averaging several spectra from Kennicutt's sample [21]. The spectra are then cross-correlated within their common rest-wavelength intervals with a template of the bulge of M31 which provides a reliable zero-point of the redshift scale [22]. We emphasise that we do *not* use the comparison of the cross-correlation with the different galaxy types for determination of the spectral types of the ESS galaxies: this technique is subject to large errors because it is very sensitive to the noise and spurious features in the spectra. Our spectral classification method is described in § 4.2 below.

The full MIDAS routine guarantees a well-controlled and user-friendly reduction of the numerous images containing simultaneous spectra of 10 (with EFOSC1) to 30 (with EMMI) galaxies. The average slit lengths vary between ~ 10 and ~ 30 arcsec and the slit width is in the range 1.3–1.8 arcsec. The dispersion is 230 Å/mm. The resolution of the resulting spectra varies from 20 Å (EFOSC1) to 10 Å (EMMI) (~ 110 spectra were obtained with EFOSC1 at the 3.6-m, the rest with EMMI at the NTT). The resulting wavelength coverage is 4300–7000 Å with EFOSC1 and 3500–9000 Å with EMMI. The signal-to-noise ratio of the spectra varies in the range 4–40, with 75% in the spectra in the range 10–30. The resulting r.m.s. uncertainty errors in the redshifts are in the range 0.0002 to 0.0005 (i.e. ~ 60 to 150 km s^{-1} ; this corresponds to a spatial scale of $1 h^{-1} \text{ Mpc}$, which is small compared to the size of the large-scale structures). For each galaxy, the rest-wavelength interval results from the combination of the grism dispersion, the position of the object within the multi-aperture mask, and the object redshift. The majority of the EFOSC1 spectra have rest-wavelength intervals in the range 3300–4700 Å, and the EMMI spectra in the range 3300–5700 Å. Therefore, only few emission-line galaxies have $H\alpha$ within the observed wavelength range.

Typical spectra of the ESS in the interval 3700–5350 Å are shown in Figure 2 (black lines). The prominent H (3968.5 Å) and K (3933.7 Å) lines of Ca II and the G molecular band of CH (4304.4 Å) are detected in most spectra with no emission lines. A large part of the contribution to the cross-correlation peak originates from these lines. A large fraction (48%)

of the galaxies in the sample have emission lines [23]. These are essentially [OII] 3727 Å, H β 4851 Å and [OIII] 4958.9 Å and 5006 Å. For objects with emission lines, the final redshift is obtained by the weighted mean of the cross-correlation redshift with the emission redshift derived by gaussian fits to the emission lines. Among the 277 galaxies for which the spectral classification has already been performed (see § 4.2), 4 are most likely HII galaxies (based on diagnostic diagrams using line ratios), and only one galaxy is a Seyfert 2 [23]. This is in marked disagreement with the significantly larger fraction of active galaxies found in the Canada-France Redshift Survey at $z \leq 0.3$ [24].

A large fraction of the ESS spectra ($\sim 3/4$) were observed in spectro-photometric weather conditions. Note that optimisation of the multi-slit spectroscopic observations does not allow to minimise the flux losses by adjusting the slit width and slit orientation (to correct for atmospheric refraction): the slit width is fixed and varies from 1.3 to 1.8 arcsec for the survey, and the slit/mask orientation is chosen as to globally maximise the spacings between the objects perpendicular to the dispersion direction. However, at the redshift of the ESS galaxies ($z > 0.1$), the slits used contain $> 95\%$ of the disk and bulge emission of a typical face-on spiral galaxy ($\sim 20 \text{ kpc}$ in diameter). Therefore, the aperture and orien-

tation bias which affect the nearby redshift surveys as well as the intermediate distance multi-fiber surveys, are small for the ESS. Comparison of multiple spectroscopic observations for a subsample of 40 spectra shows that for those taken in spectro-photometric conditions, the total external error is of the order of 7% pixel-to-pixel. Because the only existing flux-calibrated samples of galaxies are nearby samples of several tens of spectra [21], the ESS spectra provide a unique database of galaxy spectra representative of the galaxy populations in a significant spatial volume. These spectra will be useful for constraining at low redshift the models of spectrophotometric evolution of galaxies, which is an essential step for making reliable predictions of galaxy evolution at high redshift.

4. Current Results

4.1 Large-scale structure

The ESS allows for the first time to map in detail the large-scale clustering at $z \leq 0.5$ (nearly 10 times deeper than the nearby maps of the galaxy distribution [2]). Figure 3 shows the spatial distribution for ~ 400 galaxies of the ESS in 3 portions because of the long line-of-sight (the right cone shows the full redshift range for the ESS). These maps reveal a highly structured distribution which closely resembles that seen in the

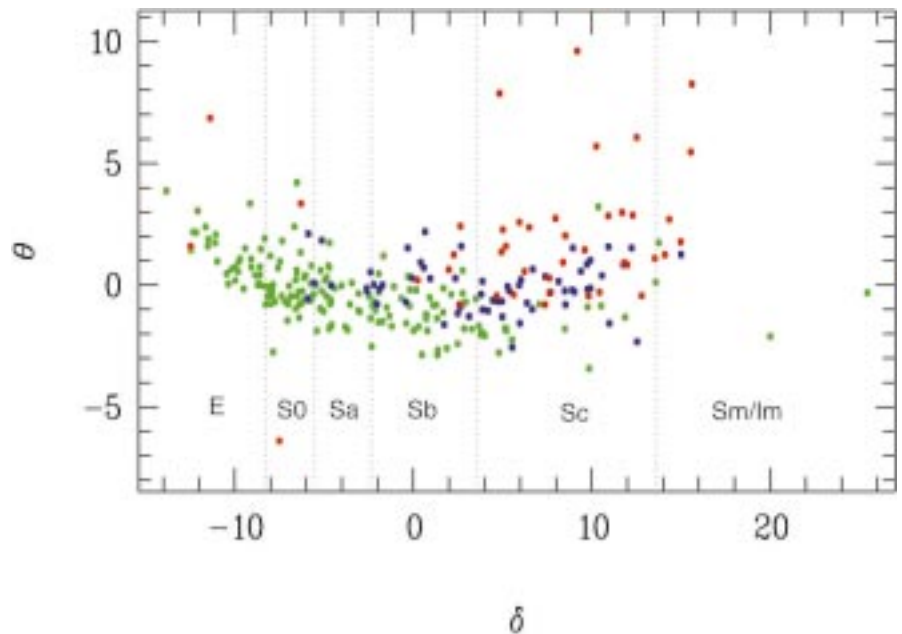


Figure 4: PCA spectral sequence for 277 ESS galaxies. The parameter δ measures the relative contribution of the red and blue stellar components in the galaxy (PC1 et PC2 in Figure 5), and θ measures the contribution of the emission lines (as shown in PC3 in Figure 5). Green points indicate galaxies with $W[\text{OII}] \leq 15 \text{ \AA}$, blue points are galaxies with $15 \text{ \AA} \leq W[\text{OII}] \leq 30 \text{ \AA}$, and red points are galaxies with $W[\text{OII}] \geq 30 \text{ \AA}$. The different discrete classes obtained by comparison with the Kennicutt spectra [21] are indicated by vertical dotted lines. Note the non-uniform sampling of the various types, with late-type galaxies spanning a larger range in δ , in good agreement with the larger variations in morphological properties among the spiral galaxies. As expected, late spectral types tend to have more frequent and stronger emission lines. θ is a good indicator of emission-line strength for late-type galaxies when used in conjunction with δ . Some of the early-type objects also have emission lines [23].

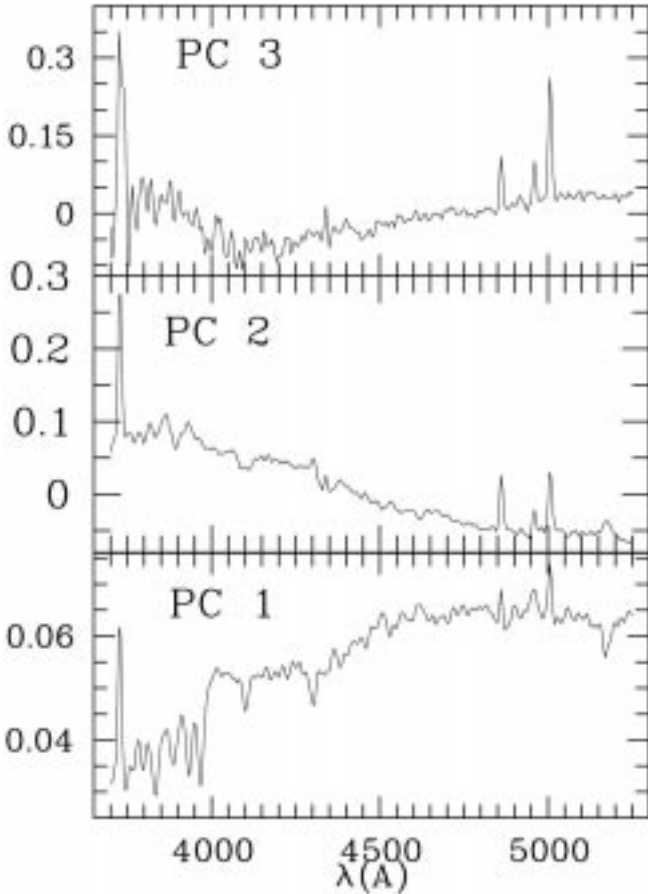


Figure 5: The first 3 principal components obtained for the ESS sample. The 1st PC is the average spectrum and resembles an Sb spectrum. The 2nd PC allows to quantify the relative contribution of the young stellar population, and the 3rd PC measures the contribution from the emission lines. 98% of the flux of the ESS spectra can be reconstructed by linear combination of these 3 PCs [23].

nearby surveys: the distribution is characterised by an alternation of sharp walls which are spatially extended across the sky, with voids with typical diameters of $20\text{--}60 h^{-1}$ Mpc [25]. The ESS maps suggest that the cell-like galaxy clustering seen in the shallower redshift surveys extends to $z \approx 0.5$. Several statistical analyses of the data are in preparation (two-point correlation function, power-spectrum, genus, etc. . .) and will provide a characterisation of the large-scale clustering in the ESS for comparison with the nearby galaxy distribution. The long line-of-sight sampled by the ESS might also provide new constraints on the galaxy clustering on scales of $\geq 100 h^{-1}$ Mpc, which are poorly sampled by the shallower surveys.

We emphasise that the large-scale structure pattern detected in the ESS is nowhere as regular as in the redshift survey of Koo et al. [26], which suggests a periodic distribution of dense structures with a separation of $128 h^{-1}$ Mpc. This scale is well above the typical size of the voids in both the shallower surveys [2, 4, 5] and the ESS. This disagreement can be partly explained by the narrow beam size of the Koo et al. probes ($\sim 5 h^{-1}$ Mpc at $z \sim 0.4$) which makes them sensitive to small-scale clustering and might cause an overestimation of both the density contrast of the walls and the size of the voids. Moreover, the sparse distribution of the narrow probes of Koo et al. over the sky

(only a few per cent of the galaxies in the survey region have a measured redshift) makes it difficult to establish a relationship between the detected peaks and the network of sheets and voids. In contrast, the ESS was designed to sample efficiently structures similar to those found in the nearby surveys: at the median redshift of 0.3, the redshift survey probes an area of $4 \times 15 h^{-1}$ Mpc², sufficient for detecting most sheets with a

surface density comparable to that for the “Great Wall” [3]. Note that the ESS lies 7° away from the Koo et al. survey on the sky. At $z \approx 0.3$ this corresponds to $90 h^{-1}$ Mpc (with $q_0 = 0.5$). Comparison of the 2 surveys shows no obvious correlation in the occurrence of the overdense structures along the line-of-sight, which might be difficult to reconcile with a typical clustering scale of $128 h^{-1}$ Mpc. Further investigations along this line using simulated distributions are in progress.

4.2 Spectral classification

In the ESS, galaxies have diameters ≤ 12 arcsec. As a result, the disk and spiral arms are poorly visible. Any attempt for a morphological classification would thus be largely approximative, and could only be limited to the presence of the main features (disk, bulge, spiral arms, signs of interaction), and restricted to the closest objects (to $z \leq 0.2$; at larger distances, the diameter of the objects becomes too small – < 9 arcsec – for any usable classification). Even from high-resolution images, the morphological classification is dependent on the filter used for the imaging, and different filters show different stellar components with varying morphologies [27]. The Spectral Energy Distributions (SED hereafter) are a useful alternative approach for characterising the galaxy populations. The SEDs measure quantitatively the relative contributions of the underlying stellar components and constrain the gas content and average metallicity. The spectral classification thus provides a physical sequence which can be interpreted in terms of evolution of the stellar components, and allows to trace back the episodes of stellar formation. For deriving a robust classification

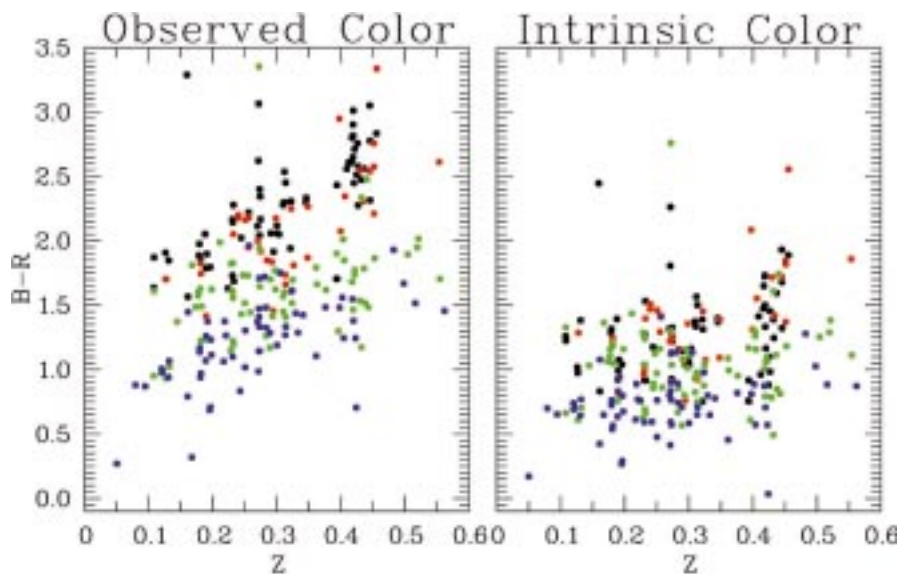


Figure 6: Observed and intrinsic $B - R$ colours for 330 ESS galaxies as a function of redshift and spectral type ($E/S0$ in black; Sa in red; Sb in green; Sc/Im in blue). The differences result from application of the K -corrections derived per spectral type, redshift interval, and filter band, using the spectrophotometric model PEGASE [34].

for the ESS, we have used the Principal Component Analysis (PCA hereafter) [28]. This technique is un-supervised in the sense that it does not rely on the use of a set of galaxy templates. It provides an objective study of the systematic and non-systematic trends of the sample, and has the advantage of being poorly sensitive to the noise level in each spectrum. Moreover, the resulting spectral classification is strongly correlated with the Hubble morphological type [29, 30, 23].

Application of the PCA to the ESS allows to re-write each spectrum as a linear combination of a reduced number of parameters and vectors (3 in this case), and which accounts for 98% of the total flux in each spectrum. The spectral type of the galaxies can be written in terms of 2 independent parameters δ , θ which respectively measure the position of the spectra along the sequence of spectral types, and the deviation from the sequence originating from either peculiar continua and/or strong emission line. The two parameters are in addition correlated (late-types tend to have stronger emission lines). Figure 4 shows the δ - θ sequence for 277 galaxies of the ESS sample. Figure 5 shows the first 3 principal components obtained from these data sets (PC1, PC2, and PC3). The first 2 principal components account for the red and blue stellar populations in the observed galaxies, and their relative contributions to each galaxy spectrum define its position along the PCA sequence (measured by δ); the 3rd component determines the emission line contribution (measured by θ). It was already known that the colours of galaxies can be described by a linear combination of stellar colours (namely types AV and M0III [31]). The interest of the PCA is to provide a more detailed demonstration of this effect over a large sample of galaxy spectra.

The continuous PCA spectral sequence obtained for the ESS can be binned to provide the corresponding fractions of the different Hubble morphological types (the correspondence is made by using spectra of galaxies with known morphology [21]). In this manner, we find that the ESS contains 17% of E, 9% of S0, 15% of Sa, 32% of Sb, 24% of Sc, and 3% of Sm/Im (see Fig. 4). The type fractions show no significant variations with redshift over the redshift range $0.1 < z < 0.5$, and are in good agreement with those found from other surveys to smaller or comparable depth (see [23, 32]). We find systematic variations in the main spectral features (equivalent width of the [OII], [OIII] and H_β emission lines; height of the 4000 Å break; slope of the continuum) with PCA spectral type, which illustrates the efficiency of the PCA technique for performing a physically meaningful spectral classification.

The PCA spectral classification has

many advantages over other classification methods. It first provides a *continuous* classification in a 2-parameter space, which allows quantitative analyses of the sample properties as a function of spectral type. In particular, it will allow an unprecedented measurement of the morphology-density relation [33] at large distance. The PCA also provides a convenient filtering technique: the reconstructed spectra (with 3 components) are inherently “noise-free” because the principal components are derived from a large sample of spectra. For the ESS, the reconstructed spectra have a signal-to-noise in the range 35–80 (to be compared with the range of 4–40 for the S/N of observed spectra). The ESS spectra are reconstructed from the principal components of Figure 5 as a linear combination $\alpha_1 \mathbf{PC1} + \alpha_2 \mathbf{PC2} + \alpha_3 \mathbf{PC3}$ (with $0.92 < \alpha_1 < 1$, $-0.2 < \alpha_2 < 0.3$, $-0.05 < \alpha_3 < 0.15$). Figure 2 shows the reconstructed spectra (in red) versus the observed spectra (in black) for 27 ESS galaxies. Reconstruction of noise-free spectra can be especially useful for comparing the ESS spectra with synthetic templates obtained from models based on stellar population synthesis [34].

The spectral classification for the ESS allows to derive accurate cosmological K-corrections for the various photometric bands, which correct for the “blue-shift” of the *observed* filter bands with respect to the *rest-frame* spectra. The crucial step is the extrapolation of the observed spectra in the rest-frame B band, which at $z \sim 0.5$ corresponds to a U filter. For this, we use the multi-spectral model PEGASE developed at IAP by B. Rocca-Volmerange et al. [34] which provides galaxy SEDs from the UV to

the infrared. These represent a good match to the ESS spectra in the optical range 3700–5250 Å. We can then derive analytical relations between galaxy spectral type as measured by δ , redshift and K-correction [32]. In turn, the K-corrections provide absolute magnitudes for the galaxies in the rest-frame filter bands. Figure 6 shows the observed $B - R$ colours for the ESS spectra as a function of redshift and spectral type and the intrinsic colours after application of the K-corrections. These diagrams show that the effect of the K-corrections on the object colours is significant over the redshift range for the ESS, and is strongly correlated with spectral type. Note, however, that the large dispersion in the observed $B - R$ colours makes any attempt to determine spectral types from colour-redshift diagrams subject to large uncertainties. This approach is often used for determination of the galaxy types.

4.3 Luminosity function

In addition to the physical information which it provides, the galaxy luminosity function is indispensable for any statistical study of an apparent magnitude-limited survey. However, this function is poorly known so far due to the limited samples adequate for its measurement. The existing luminosity functions measured at $z \leq 0.2$ from surveys with typically $\sim 10^4$ galaxies give variables results, which are a function of the selection criteria for the samples [32]. The “local” luminosity function ($z \sim 0.03$) [35] is likely to be affected by errors in the magnitude measurements in the Zwicky catalogue. Luminosity functions based on digitised plates can be biased by the non-linearity

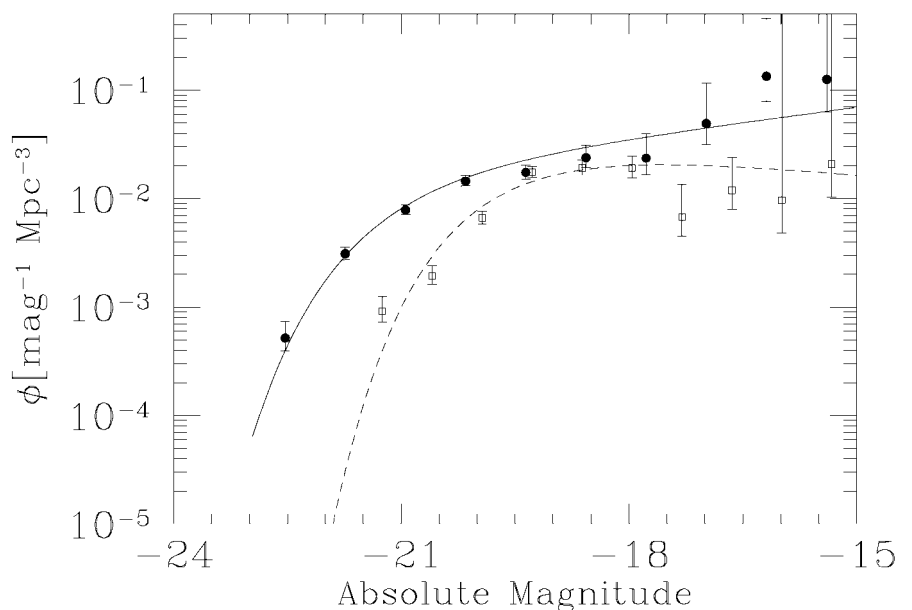


Figure 7: Luminosity functions in B (open squares) and R (filled circles) for 327 galaxies of the ESS. The best fit Schechter functions have $M_B^* = -19.58 \pm 0.17$, $\alpha_B = -0.85 \pm 0.17$, and $M_R^* = -21.15 \pm 0.19$, $\alpha_R = -1.23 \pm 0.13$ [32].

of the photographic emulsion at bright magnitudes [36], and by incompleteness at faint magnitudes. The recent Las Campanas Redshift Survey [4] has the advantage of providing the largest CCD galaxy catalogue for measurement of the luminosity function at $z \sim 0.2$ (see [37] and references therein). However, this spectroscopic sample is affected by selection effects such as variable sampling over the sky, and a systematic under-sampling of low-surface brightness galaxies, which might be responsible for the shallow faint-end slope.

The luminosity functions for different galaxy types show variations in their faint end slopes [37, 35]; in some cases, the variation is closely related to the presence of emission lines in the galaxy spectra [38]. In addition, deep redshift surveys suggest that the slope of the late-type luminosity function evolves significantly at $z \geq 0.5$ [39, 40, 41]. Although the different deep surveys agree to detect an evolution in the luminosity density by a factor of nearly 2 between $z \sim 0$ et $z \geq 0.5$ [41, 42], the differences in the results emphasise the need for a confrontation with new catalogues. In Figure 7, we show the B and R luminosity function for 327 galaxies from the ESS sample calculated using an “inhomogeneity-independent” method (see [32] for details). The 2 luminosity functions are in good agreement with the results for the CNOC1 survey [40] using similar filters and an analogous observational set-up (multi-slit spectroscopy at the Canada-France-Hawaii telescope), and which probes the galaxy distribution to similar depth as the ESS. A more detailed study using the full ESS sample is in course.

5. Conclusions and Prospects

The ESS demonstrates the interest of a deep fully-sampled pencil-beam survey for probing through and identifying numerous large-scale structures along the line-of-sight. The survey confirms that the nearby properties of the large-scale clustering extend to $z \lesssim 0.5$, namely a cell-like structure of sharp walls alternating with voids of order of 20–60 h^{-1} Mpc in diameters [25]. Measures of the power-spectrum at scales $\geq 100 h^{-1}$ Mpc and of the topological properties of the detected structures will provide useful constraints on the nature of the primordial fluctuations which led to the observed large-scale clustering. The ESS also has the potential for uncovering very large structures exceeding the extent of the shallower surveys. Some marginal evidence for the presence of an extended under-density in the redshift range 0.3–0.4 is under close examination.

The ESS photometric survey is the largest CCD multi-colour survey of galaxies, and allows to confirm with tighter

error bars the previous analyses of galaxy number counts and colour distribution at $B < 24.5$ based on smaller areas and/or fewer bands [17]. The ESS galaxy spectra provide a unique database for adjustment of the models of spectrophotometric evolution of galaxies at “low” redshift [34]. Calibration of these models on the ESS data, via the proportions of the different galaxy types and their luminosity functions will allow to obtain better predictions of galaxy evolution at $z > 1$. These predictions could be tested on the full photometric sample, which extends significantly deeper than the spectroscopic sample, using the 2-point angular correlation function [19]. Photometric redshifts techniques [42], which would require the acquisition of U -band photometry, would provide additional constraints, and are under consideration.

The ESS spectroscopic sample is being complemented by a similar spectroscopic survey being performed in the northern hemisphere using the CFH Telescope. The ~ 1700 galaxies contained in the two samples, and their homogeneous spectral classifications and absolute magnitude determinations provided by the Principal Component Analysis [23] will provide a new measure of the luminosity function as a function of spectral class at the intermediate redshifts $0.1 \leq z \leq 0.5$. The difficulty to interpret the galaxy number-counts from the “Hubble Deep Field” [42] emphasises the need for a better determination of the “local” luminosity function per galaxy type. Objective detection of the galaxy groups within the ESS is also in progress and will allow a detailed study of the different galaxy populations and their relationship with the environment, as measured by the local galaxy density and the location within the large-scale structure. In particular, the morphology-density relation [33], and the existence of an analogous to the Butcher-Oemler effect [43] for field galaxies are being investigated.

The optical study of the ESS data is complemented by multi-wavelength follow-up observations: IRAC2 on the ESO-2.2-m telescope is used for obtaining K' imaging of a sub-sample of the ESS spectroscopic sample; the same region is scheduled for observations with ISO at 10 μm and 90 μm (in collaboration with B. Rocca-Volmerange); the full ESS region has been observed with the VLA at 6 cm and 20 cm (in collaboration with J. Roland and A. Lobanov). The optical- K' colours allow to identify the stellar populations from massive stars to old giants. The K' -far-infrared colours allow to separate the different populations of grains, and indirectly allow to constrain the star-formation rate. Determination of the luminosity functions per type in the infrared, are crucial for interpreting the infrared galaxy counts. These, in contrast to the optical counts,

show no excess over no-evolution models [44]. Finally, the radio observations will allow to study the correlation between the optical and radio properties of the different galaxy populations in an optically selected sample (the opposite of the usual approach of making optical follow-up observations of a radio-selected sample).

We are considering the extension of the ESS spectroscopic sample one magnitude fainter using FORS1 at the VLT/UT1. This would provide the redshifts for another ~ 1000 galaxies to $z \lesssim 1$ for which the photometry is already available. This survey would be useful for obtaining a dense sampling of the large-scale structure at redshifts where so far only individual structures are detected, usually in association with quasars or radio galaxies. The evolution of the large-scale clustering at $z \sim 1$ is expected to depend markedly on the cosmological parameters [45]. Any detection or absence of evolution in the cell-like pattern with redshift would provide useful constraints on the mean matter density in the Universe (Ω). The redshift extension of the ESS would also be useful for preparing the definition of the large area surveys which will be done more efficiently with VIRMOS.

Only one other systematic redshift survey is currently being performed at the depth of the ESS: the CNOC2 programme, with the goal to obtain redshifts for 10,000 galaxies at $z \lesssim 0.7$. Answering the question of the scale of homogeneity in the galaxy distribution, and hence of the underlying matter distribution will nevertheless require larger area redshift surveys than the ESS and CNOC2. In particular, the “Sloan Digital Sky Survey” (SDSS) [46] and the “2dF” project [47] to map 1 million and 250,000 galaxies respectively out to distances $z \sim 0.2$ over large areas of the sky will both make a tremendous improvement in the statistical analysis of the galaxy distribution. The larger distances will be probed by the 2dF extension (6,000 galaxies to $R \approx 21$) [47] and the DEEP survey with the Keck Telescope (15,000 galaxies with $B \lesssim 24$) [48]. Note that the well-known difficulties with the flux calibration of multi-fiber spectroscopy, supplemented by the aperture bias at $z \lesssim 0.2$ (the fibres only sample the core of the galaxies) will make any spectral classification of the SDSS and shallow 2dF survey subject to a number of biases. A unique survey for determination of the galaxy luminosity function per type will be the 5-m “Liquid-mirror telescope” which will provide SEDs with photometric quality for nearly one million galaxies to $z \sim 1$ using a multi-narrow-band imaging technique [49]. These data will be essential for constraining the evolution of the galaxy populations and of the large-scale clustering with look-back time. It will also allow to simulate the biases in the SEDs obtained with the

multi-fibre surveys. Although the ESS is not in proportion with these large-area surveys to come in terms of survey volume, budget, and manpower, it provides an anticipated understanding of the properties of the galaxy distribution at large distances.

Acknowledgements

We are grateful to ESO for the numerous nights of observing time allocated to this programme. We also wish to thank the staff members in La Silla who greatly contributed to the success of our observing runs. This research is partly supported by the "Programme National de Cosmologie" (previously "GdR Cosmologie") from INSU/CNRS.

References

- [1] Oort, J.H. 1983, *Ann. Rev. of Astron. and Astroph.*, **21**, 373.
- [2] de Lapparent, V., Geller, M.J., Huchra, J.P. 1986, *Astroph. J. Lett.*, **302**, L1.
- [3] Ramella, M., Geller, M.J., & Huchra, J.P., 1992, *Astroph. J.*, **384**, 396.
- [4] Shectman, S.A., Landy, S.D., Oemler, A., Tucker, D.L., Kirshner, R.P., Lin, H., & Schechter, P.L. 1996, *Astroph. J.*, **470**, 172.
- [5] Vettolani, G., Zucca, E., Zamorani, G., Cappi, A., Merighi, R., Mignoli, M., Stirpe, G.M., MacGillivray, H., Collins, C., Balkowski, C., Cayatte, V., Maurogordato, S., Proust, D., Chincarini, G., Guzzo, L., Maccagni, D., Scaramella, R., Blanchard, A., Ramella, M. 1997, *Astron. & Astroph.*, in press.
- [6] Schuecker, P. & Ott, H.-A. 1991, *Astroph. J. Lett.*, **378**, L1 (<http://aquila.uni-muenster.de/mrsp-overview.html>).
- [7] Bahcall, N.A., Lubin, L.M., & Dorman, V. 1995, *Astroph. J. Lett.*, **447**, L81.
- [8] Dar, A. 1995, *Astroph. J.*, **449**, 553.
- [9] Blumenthal G.R., Faber, S.M., Primack, J.R., & Rees, M.J. 1984, *Nature*, **311**, 517.
- [10] Brdeen, J.M., Bond, J.R., Kaiser, N., Szalay, A.S. 1986, *Astroph. J.*, **304**, 15.
- [11] Brosch, N. 1989, *Astroph. J.*, **344**, 597.
- [12] Kuhn, B., Hopp, U., Elsaesser, H. 1997, *Astron. & Astroph.*, **318**, 405.
- [13] Bennett, C.L., Banday, A.J., Gorski, K.M., Hinshaw, G., Jackson, P., Keegstra, P., Kogut, A., Wilkinson, D.T., Wright, E.L. 1996, *Astroph. J. Lett.*, **464**, L1.
- [14] Ashman, K.M., Salucci, P., Persic, M. 1993, *M.N.R.A.S.*, **260**, 610.
- [15] Madau, P., Ferguson, H.C., Dickinson, M.E., Giavalisco, M., Steidel, C.C., Fruchter, A. 1996, *M.N.R.A.S.*, **283**, 1388.
- [16] Santiago, B.X., da Costa, L.N. 1990, *Astroph. J.*, **362**, 386.
- [17] Arnouts, S., Lapparent, V., Mathez, G., Mazure, A. & Mellier, Y., Bertin, E. & Kruszewski, A. 1997, *Astron. & Astroph. Suppl.*, **124**, 163.
- [18] Bertin, E. & Arnouts, S. 1996, *Astron. & Astroph. Suppl.*, **117**, 393.
- [19] Arnouts, S., Thèse de Doctoral, Université Paris VII, 1996.
- [20] Metcalfe, N., Shanks, T., Campos, A. & Fong, R. 1996, *Nature*, **383**, 236.
- [21] Kennicutt, R.C. 1992, *Astroph. J. Suppl.*, **79**, 255.
- [22] Bellanger, C., de Lapparent, V., Arnouts, S., Mathez, G., Mazure, A. & Mellier, Y., 1995, *Astron. & Astroph. Suppl.*, **110**, 159.
- [23] Galaz, G. & de Lapparent, V., 1997, *Astron. & Astroph.*, submitted.
- [24] Tresse, L., Rola, C., Hammer, F., Stasinska, G., Le Fèvre, O., Lilly, S.J., Cramp-ton, D. 1996, *M.N.R.A.S.*, **281**, 847.
- [25] Bellanger, C., de Lapparent, V., 1995, *Astroph. J. Lett.*, **455**, L103.
- [26] Koo, D.C., Ellman, N., Kron, R.G., Munn, J.A., Szalay, A.S., Broadhurst, T.J. & Ellis, R.S., 1993, in *Observational Cosmology*, eds. G. Chincarini et al., *ASP Conf. Ser.*, Vol. **51**, 112.
- [27] O'Connell, R.W., Marcum, P. 1996, in *HST and the High Redshift Universe (37th Hertstmonceux Conference)*, eds. N.R. Tanvir, A. Aragon-Salamanca, & J.V. Wall.
- [28] Murtagh, F. & Heck, A. 1987, *Multivariate Data Analysis*, Reidel.
- [29] Connolly, A.J., Szalay, A.S., Bershad, M.A., Kinney, A.L. & Calzetty, D. 1995, *Astron. J.*, **110**, 1071.
- [30] Sodré, L. & Cuevas, H. 1994, *Vistas in Astronomy*, **38**, 287.
- [31] Aaronson, M. 1978, *Astroph. J.*, **221**, L103.
- [32] Galaz, G., Thèse de Doctoral, Université Paris VII, 1997.
- [33] Dressier, A. 1980, *Astroph. J.*, **236**, 351.
- [34] "Base de données PEGASE", 1996, A.A.S. CD-ROM Series, Vol. **7**, ed. Leitherer et al. (<http://www.iap.fr/users/rocca/index.html>)
- [35] Marzke, R.O., Geller, M.J., Huchra, J.P. & Corwin, H.G., Jr 1994, *Astron. J.*, **108**, 437.
- [36] Bertin, E. & Dennefeld, M. 1997, 1997, *Astron. & Astroph.*, **317**, 43.
- [37] Lin, H., Kirshner, R.P., Shectman, S.A., Landy, S.D., Oemler, A., Tucker, D.L. & Schechter, P.L. 1996, *Astroph. J.*, **464**, 60.
- [38] Zucca, E., Zamorani, G., Vettolani, G., Cappi, A., Merighi, R., Mignoli, M., Stirpe, G.M., MacGillivray, H., Collins, C., Balkowski, C., Cayatte, V., Maurogordato, S., Proust, D., Chincarini, G., Guzzo, L., Maccagni, D., Scaramella, R., Blanchard, A., Ramella, M. 1997, *Astron. & Astroph.*, in press.
- [39] Heyl, J., Colless, M., Ellis, R.S. & Broadhurst, T., 1997, *M.N.R.A.S.*, in press, (astro9610036).
- [40] Lin, H., Yee, H.K.C., Carlberg, R.G., Ellingson, E. 1997, *Astroph. J. Lett.*, **475**, 494.
- [41] Lilly, S.J., Tresse, L., Hammer, F., Crampton, D. & Le Fèvre, O., 1995, *Astroph. J.*, **455**, 108.
- [42] Sawicki, M.J., Lin, H., Yee, H.K.C. 1997, *Astron. J.*, **113**, 1.
- [43] Butcher, H. & Oemler, A. 1978, *Astroph. J.*, **219**, 18.
- [44] Cowie, L.L., Gardner, J.P., Hu, E.M., Songaila, A., Hodapp, K.-W., Wainscoat, R.J. 1994, *Astroph. J.*, **434**, 114.
- [45] White, S.D.M. 1997, in *The Early Universe with the VLT*, ed. J. Bergeron (Springer-Verlag).
- [46] <http://www-sdss.fnal.gov:8000/>
- [47] <http://msowwww.anu.edu.au/colless/2dF/>
- [48] <http://www.ucolick.org/deep/home.html>
- [49] <http://www.astro.ubc.ca/LMT/lmt.html>

V. de Lapparent
lapparen@iap.fr

Massive Stars Running Through Space

L. KAPER, F. COMERÓN, J.Th. VAN LOON, A.A. ZIJLSTRA

1. Introduction

OB runaways are massive (OB) stars that travel through interstellar space with anomalously high velocities. The space velocity of these stars can be as high as 100 km/s, which is about ten times the average velocity of "normal" OB stars in the Milky Way. Many of them can be traced back to a nearby OB association where they seem to have originated from. But how did these massive stars obtain such a high velocity? Recent observations carried out at the European Southern Observatory have provided

compelling evidence that, at least in one case, the supernova explosion of a massive binary companion is responsible for the large space velocity gained by the remaining OB star. The observational evidence is based on the discovery of a wind bow shock around the high-mass X-ray binary Vela X-1, an X-ray pulsar with a B-supergiant companion. Here we report on new high-resolution coronagraphic observations of the bow shock obtained with ESO's *New Technology Telescope*. Furthermore, we present the first results of hydrodynamical calculations simulating the interaction between

the interstellar medium and the stellar wind of a B supergiant moving with a supersonic velocity.

According to Blaauw (1961), a "bona-fide" runaway star fulfils two criteria: (i) it has an observed high (i.e. > 30 km/s) space velocity and (ii) a "parent" OB association has been identified. It turns out that a significant fraction of the OB stars are runaways; their frequency steeply decreases as a function of spectral type: from about 20% among the O-types to 2.5% among B0-B0.5, and still lower among B1-B5 (Blaauw, 1993). Almost all runaways appear to be single;